Ionization and acceleration processes in a small, variable channel width, permanent-magnet Hall thruster

2012 J. Phys. D: Appl. Phys. 45 185203

(http://iopscience.iop.org/0022-3727/45/18/185203)

IOP PUBLISHING JOURNAL OF PHYSICS D: APPLIED PHYSICS

J. Phys. D: Appl. Phys. **45** (2012) 185203 (7pp) doi:10.1088/0022-3727/45/18/185203

Ionization and acceleration processes in a small, variable channel width, permanent-magnet Hall thruster

S Mazouffre, G Bourgeois, K Dannenmayer and A Lejeune

ICARE, CNRS, 1C avenue de la Recherche Scientifique, 45071 Orléans, France

E-mail: stephane.mazouffre@cnrs-orleans.fr

Received 19 December 2011, in final form 27 February 2012
Published 18 April 2012
Online at stacks.iop.org/JPhysD/45/185203

Abstract

A 200 W-class permanent-magnet Hall thruster has been operated with different channel widths. A series of experiments have been carried out for each geometry over a broad range of propellant mass flow rates and applied voltages to investigate the impact of a channel cross-section area variation on discharge and plume properties. Measurement outcomes allow calculation of several quantities, namely the propellant utilization, the beam voltage, the equilibrium wall temperature and the energy flux towards the walls. This study reveals that widening the channel of a low-power Hall thruster enhances ionization and acceleration processes and broadens the operating envelope. Two mechanisms are proposed to explain experimental observations. The surface-to-volume ratio decreases with h, which reduces wall-losses. The magnetic field strength near walls increases with h, which leads to a better plasma confinement.

(Some figures may appear in colour only in the online journal)

1. Background and objective

A Hall thruster (HT) consists of a plasma discharge in a crossed electric and magnetic field configuration [1, 2]. A low-pressure xenon plasma is generated between an internal anode and an external hollow cathode. The plasma spatial extension is limited to the interior of an annular dielectric channel. A magnetic field B, generated either by coils or permanent magnets, confines the electrons but does not much affect the ion trajectory. Electron mobility is considerably reduced near the channel exit plane where B is the strongest. The potential drop is therefore concentrated in this area. The corresponding axial electric field accelerates xenon ions, which generates the thrust. HTs operating around 1.5 kW are commonly used for orbit correction of geosynchronous satellites [2]. Low power devices could advantageously serve for drag compensation of observation satellites [3]. Moreover, high-power HTs represent an attractive option for orbit transfer maneuvers and interplanetary journeys [4]. A recent investigation on scaling laws for HTs revealed the majority of HTs are built according to a linear relation between the channel width h and the channel mean diameter d [5]. In other words, the h to d ratio stays the same whatever the thruster sizes, input power and thrust level. This means optimized HTs operate nominally at the same neutral gas density in the anode region and at a constant ion current density. The latter, however, tends to decrease at low input power due to a poor mass utilization [5].

In 1998, Raitses *et al* investigated the impact of the channel length and profile upon the performances of a 500 W-class HT with glass walls [6]. The channel cross-section was solely modified in the near anode region by means of glass spacers to tailor the electron temperature owing to a pinch effect. Authors found a narrow channel solely improves propellant utilization and thrust efficiency at low mass flow rates, i.e. when ionization is weak. In this contribution, we aim at studying the influence of the channel width on ionization and acceleration processes in a low-power HT. In order to investigate the impact of the h to d ratio on discharge properties, three sets of ceramic rings were used to modify the channel width without modifying the channel mean radius and the channel length. Several quantities have been measured over a broad range of propellant mass flow rates and applied voltages for the three channel configurations, namely the discharge current, the ion current density in the plume, the Xe^+ ion axial velocity profile, the ion energy in the plume far-field and the channel wall temperature. As we shall see throughout the next

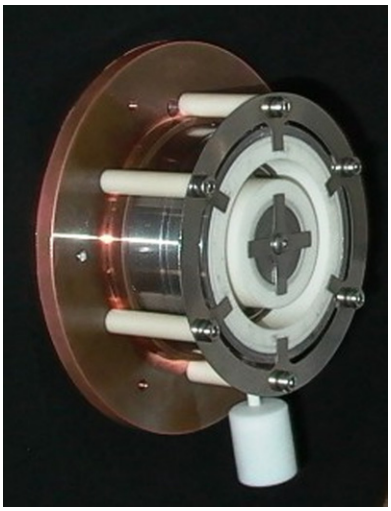

Figure 1. Picture of the PPI low-power permanent-magnet Hall thruster.

sections, analysis of the complete data set reveals the channel cross-section area has a noticeable impact on a HT discharge properties and performance. Note that thrust, specific impulse and efficiency are not reported in this paper.

2. Hall thruster

2.1. Low-power permanent-magnet thruster

A 200 W laboratory model HT able to deliver a thrust of 10 mN at 250 V with 1 mg s^{-1} xenon mass flow rate has been employed for this study [7, 8]. The thruster is named PPI, a French acronym for 'Petit Propulseur Innovant'. A picture of the PPI HT is shown in figure 1. This thruster exhibits three interesting features that make it highly versatile. First, the magnetic field is generated by way of miniature SmCo magnets brought together inside rings located on either side of the channel walls. A soft iron magnetic circuit with a back gap drives the magnetic flux in order to obtain the desired topology. No magnetic screen is used. The magnetic field strength can easily be modified by varying the number of magnets. Second, the propellant gas is injected homogeneously inside the channel using a porous ceramic instead of a classical metal hollow gas injector. A stainless-steel ring placed at the back of the channel serves as anode. Third, a central copper heat drain is employed to evacuate heat towards a radiator placed behind the thruster. During operation at 200 W, the inner magnet steady-state temperature is 200 °C, well below the Curie point.

A special version of the thruster was designed in which the channel width h can be easily modified while keeping the mean diameter d unchanged [9]. Three channel widths were realized by installing three sets of alumina rings, such that the channel cross-section area is either S_0, two times S_0 or three times S_0, wherein $S_0 = \pi h_0 d_0$ corresponds to the value of standard HTs. In this paper, the three-channel geometries are labelled S_0, $2S_0$ and $3S_0$, respectively. Figure 2 depicts in broad outline the three channel configurations as well as the magnetic field amplitude along the channel radius. Although the magnetic field map was unchanged during all experiments,

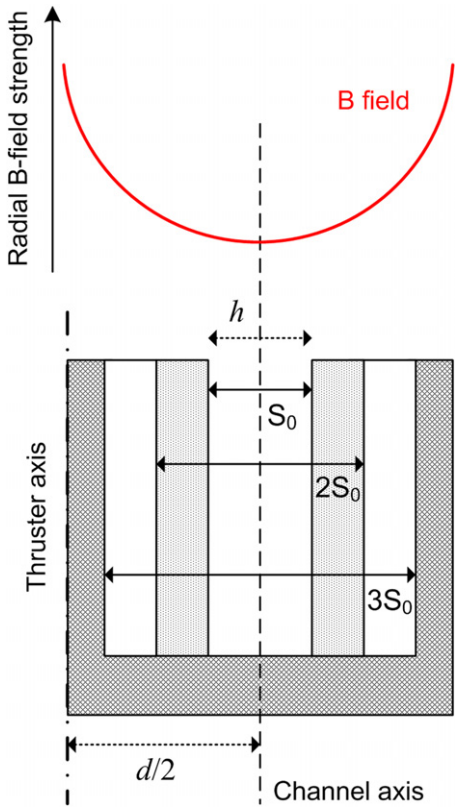

Figure 2. Schematic of the thruster acceleration channel showing the three geometries. Also shown is a sketch of the B-field strength along the radius.

with the highest on-axis magnitude at the channel exit plane, the drawing shows the magnetic field gradient and strength at the channel boundaries depends upon the ceramic ring set. The fact that Al_2O_3 rings are used is not decisive for the purpose of the work. Moreover, the thruster was fired at low voltages so that wall material impact is limited [10].

2.2. Operating parameter envelope

The thruster was successfully tested in the NExET facility [9] with the three geometrical configurations. An external hollow cathode with a LaB_6 insert was used as neutralizer with a constant xenon mass flow rate of 0.2 mg s^{-1}. The cathode orifice was placed 10 cm below the thruster symmetry axis and 3 cm away from the channel exit plane. When moving the cathode away from the thruster, the discharge current decreases by about 10% (e.g. 0.9 A instead of 1 A at 1 mg s^{-1} and 200 V). The cathode gas flow therefore influences the performance, yet the observed qualitative behaviour does not change. Figure 3 illustrates the operating parameter envelope, i.e. the voltage-flow rate curve, covered with each channel geometry. As can be seen, the thruster was fired over a broad range of xenon anode mass flow rates (0.4–3.1) mg s^{-1} and applied discharge voltages (50–400) V [9]. The corresponding background pressure range was (1.5–5) $\times$ 10^{-3} Pa-Xe. The pressure was measured with an ionization gauge. In terms of input power, the thruster operated between 25 and 460 W. Values above 350 W were only maintained for a short duration to limit the thermal load. We first noticed the thruster is easier

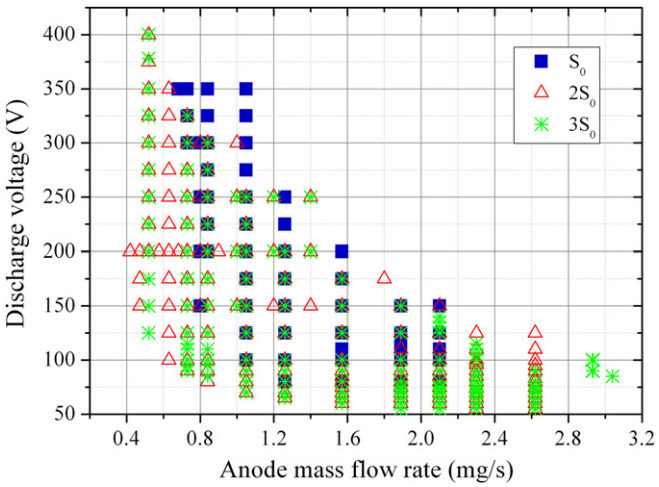

Figure 3. Influence of the channel geometry upon the mass flow rate–voltage envelope.

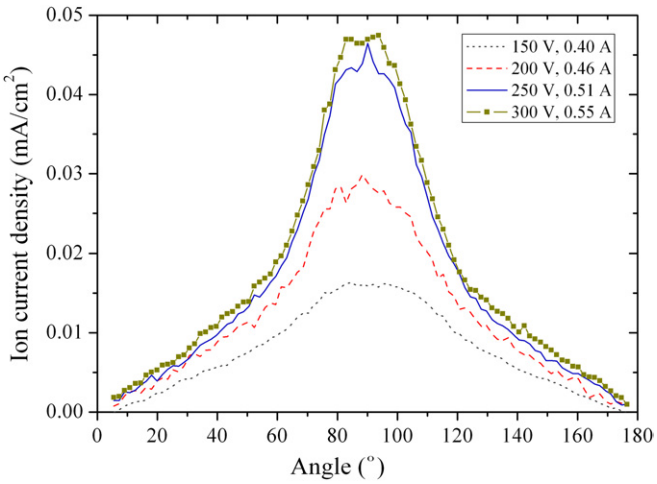

Figure 4. Plume ion current density angular profile for the PPI Hall thruster in S_0 configuration for several voltages (0.8 mg s^{-1}). The 90° angle corresponds to the thruster centreline.

to ignite with the $3S_0$ geometry, i.e. with the wider channel, whatever the operating conditions. Second, the parameter envelope is broader with the $2S_0$ and $3S_0$ configurations, as exemplified in figure 3. With a wide channel, the thruster can function at low voltage with low gas flow rates as well as at power well above the normal one.

The extended operation envelope and easy ignition support the idea that losses diminish when the channel width h increases. Operation at relatively high power is possible without trouble since the atom density that warrants a great ionization degree corresponds to a large propellant flow for a wide channel [5]. The physical mechanisms that connect channel cross-section area and performance level are critically examined in section 6 in light of well-resolved experimental data.

3. Ionization efficiency

The ion current was measured in the thruster far-field plume by means of a graphite planar Faraday probe equipped with a guard ring [9]. The probe active area is 1 cm^2. The probe was negatively biased at −50 V [11]. The current was captured with a 10 Ω load to minimize disturbance of the plasma sheath. A low-pass (35 kHz) amplifier with a gain of 10 dB delivers the output signal. The probe was located 40 cm downstream of the channel exit plane and rotated over 180°. The measured current density is typically below 0.1 mA cm^{-2}. Figure 4 shows the ion current density angular profiles acquired in the (x, z) plane with the S_0 geometry for several discharge voltages. Similar profiles are measured with the two other geometries. The tails observed at large angle with respect to the axis originate in charge-exchange collision events between fast Xe^+ ions of the beam and slow background gas Xe atoms as well as in ion scattering due to elastic collisions. As can be seen in figure 4, tails are strong despite a low residual xenon gas pressure. Charge exchange collisions are certainly favoured here as the cathode delivers a non-negligible amount of neutrals in the plume near-field.

The total ion current in the beam I_t can be computed from the experimentally measured ion current profiles assuming a cylindrical symmetry with respect to the thruster axis and a probe apparatus function with no dependence on the angle [9]. Before computing the total ion current, the current flux distribution must be corrected to suppress the effect of charge exchange collisions. In this study, the lateral spread of the ion beam profile is strongly reduced by fitting the central part of the ion distribution to a Gaussian function. Our correction method is disputable as there are several ways for correcting for the appendages of the ion profile [12, 13]. Yet the fit method will not modify the ordering of the ion current for the three geometries.

The ion mass flow rate generated by the thruster reads

$$\dot{m}_i = \frac{M}{e} I_t, \tag{1}$$

where M and e denote the atomic mass and the elementary charge, respectively. The ionization efficiency α, also called the anode propellant utilization, corresponds to the fraction of propellant gas flow rate injected through the anode that is converted into ion flow. It is given by the ratio of $\dot{m}_i$ to $\dot{m}_a$. The uncertainty in the calculation of α is large due to the necessary treatment of the ion current profile. A statistical analysis indicates an error bar of 20%. The anode propellant utilization does not account for the amount of gas flowing in the cathode. The quantity α is plotted as a function of the discharge voltage in figure 5 for the three thruster channel geometries. First, α increases with the applied voltage U_d for all geometries. The increase with U_d has two main origins: the gain in ionization probability and the growth of the multiply charged ion species fraction, especially Xe^{2+}. The ionization rate and the production yield of multiply charged ions increase with the electron temperature. The latter increase with the discharge voltage [5]. Therefore, the ion density increases on the whole with U_d, which explains the larger propellant efficiency. Second, for a given mass flow rate the ionization efficiency increases drastically with the

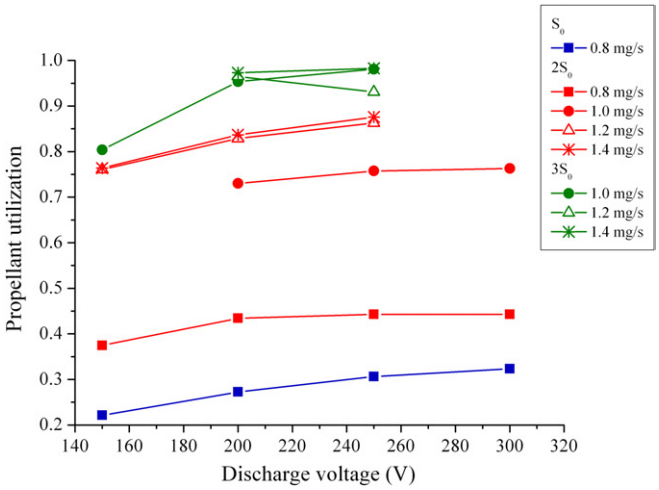

Figure 5. Anode propellant utilization as a function of the discharge voltage for the three HT geometries.

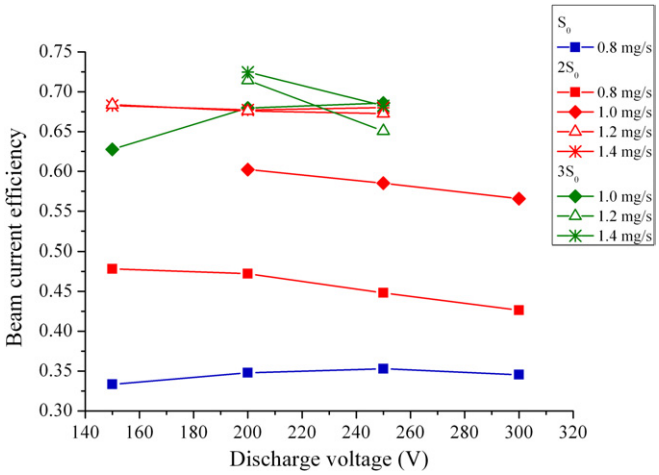

Figure 6. Beam current efficiency against the discharge voltage for the three HT geometries.

channel width h. With the $3S_0$ configuration, α is above 0.9 for $U_d > 200$ V, a value commonly reached for large thrusters. It is preferable to examine the impact of h on the propellant utilization for a fixed atom density in the channel. According to our dataset, the (S_0, 0.8 mg s^{-1}) and ($2S_0$, 1.0 mg s^{-1}) points can for instance be compared with, respectively, ($2S_0$, 1.4 mg s^{-1}) and ($3S_0$, 1.4 mg s^{-1}). As a complement to previous data, figure 6 shows the beam current efficiency, i.e. the ion current divided by the discharge current, as a function of U_d. Like the anode propellant utilization, the beam current efficiency increases as the channel is widened.

As exemplified in figure 5 and 6, the positive impact of h is obvious, although the gap reduced at large flow rates. Error bars are certainly large for calculated values of the ion current due to the arbitrary correction method for the appendages and to the fact that cathode gas flow ingestion is not accounted for. However, it is demonstrated that the ionization efficiency, and indirectly the thrust level, increases with the channel cross-section area.

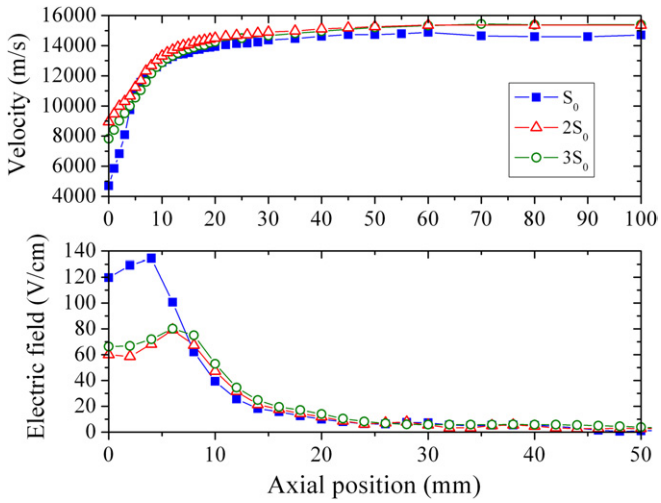

Figure 7. Influence of the channel width on Xe^+ axial velocity (top) and electric field (bottom). Conditions: 200 V, 1 mg s^{-1}. The position $x = 0$ mm refers to the channel exit plane.

4. Ion axial velocity

In order to investigate the relationship between channel geometry and ion acceleration, the Xe^+ ion velocity was measured along the channel axis by means of LIF spectroscopy. The optical bench used to probe the metastable $5d\,^2F_{7/2}$ Xe^+ state is extensively described in, e.g., [14]. A high-power tunable single-mode laser diode is used to excite xenon ions at 834.723 nm. A high-precision wavemeter monitors the laser wavelength. Laser stability is real-time checked by a 2 GHz confocal Fabry–Pérot interferometer. The laser beam passes through several optics until it reaches the thruster through a window located at the back of the NExET vacuum chamber. The laser beam is shined along the thruster channel axis. The 541.915 nm fluorescence light is collected at 90° with respect to the beam direction. A 10 nm bandwidth filter is used to isolate the fluorescence line. A photomultiplier tube serves as a radiation sensor. Lock-in detection permits improvement of the signal-to-noise ratio. The HT is mounted onto a translation stage to enable measurements at several axial positions. With the 834.723 nm optical transition, the fluorescence profile images to a large extent the Xe^+ ion velocity distribution function [14, 15]. In this study we solely consider the most probable velocity of each VDF. Assessment of the maximum of the VDF leads to a random error of ±150 m s^{-1}.

The on-axis profile of the Xe^+ axial velocity component is displayed in figure 7 for the S_0, $2S_0$ and $3S_0$ geometrical configurations. The position $x = 0$ mm refers to the channel exhaust. The three velocity profiles exhibit the same general trend. The Xe^+ ion velocity increases quickly over the first 20 mm. Ions still accelerate a little until $x = 60$ mm. Beyond this distance they travel at constant axial velocity whatever the geometry. One accesses a more accurate picture when computing the accelerating potential. The latter is obtained from conservation between kinetic energy and potential energy assuming a collisionless medium [15]. The potential drop experienced by ions inside the channel is given by the kinetic energy at the channel exit plane: it is, respectively, 15 V, 54 V

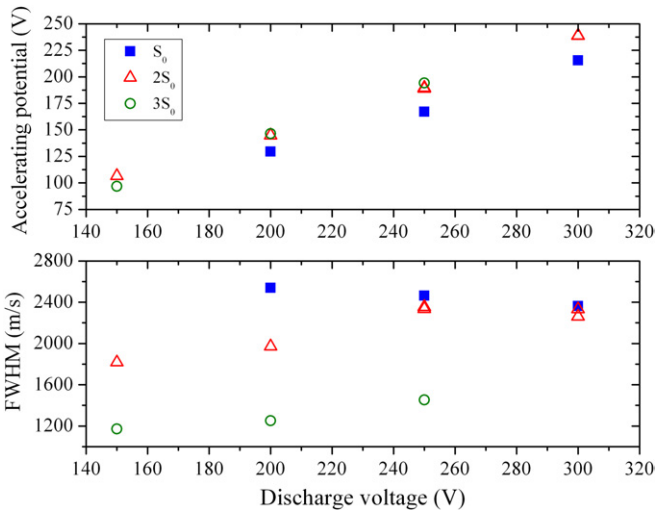

Figure 8. Accelerating potential (top) and FWHM of the velocity distribution (bottom) against discharge voltage for the three-channel geometries. ($D_a = 1\,\mathrm{mg\,s^{-1}}$).

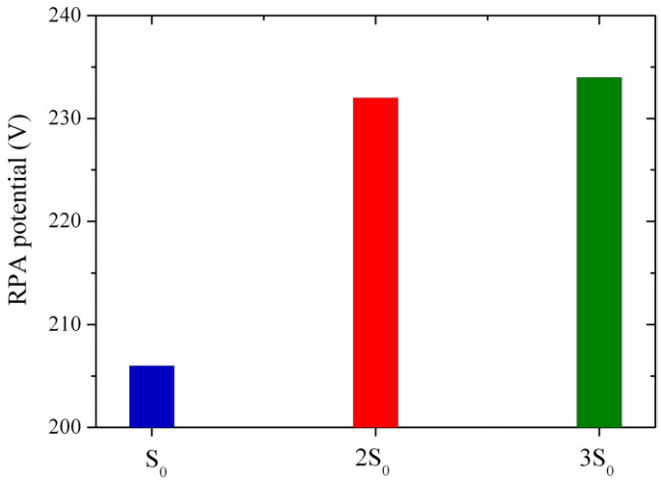

Figure 9. Evolution of the ion kinetic energy along with the thruster channel geometry (250 V, 1 mg s^{-1}).

and 41 V for the S_0, $2S_0$ and $3S_0$ configurations. The overall accelerating potential is computed from the ion final velocity. One finds 146 V for the S_0 geometry, 161 V for the $2S_0$ and 162 V for the $3S_0$ against 200 V applied voltage. The fraction of acceleration inside the channel is then 0.11, 0.33 and 0.25 for the S_0, $2S_0$ and $3S_0$, respectively. The two widest channels are more efficient for transforming input electrostatic energy into kinetic energy. This fact is clearly illustrated in figure 8 wherein the accelerating potential is plotted against U_d for a constant xenon mass flow rate. The gain is always above 15 V between the S_0 and the $2S_0$ geometry. Passage from the $2S_0$ to the $3S_0$ has almost no effect on the ion velocity. Not only does the velocity increase with h but the velocity spread also diminishes, which means that a greater number of ions are produced upstream of the acceleration region. The full-width at half-maximum of the Xe^+ ion VDF ($x = 100$ mm) is plotted as a function of U_d in figure 8.

Figure 7 also shows the development of the electric field along the channel axis. The electric field is the derivative of the accelerating potential. Note that prior to the differentiation operation each profile was smoothed through a fit to a cubic spline. The electric field magnitude is seemingly higher for the narrowest channel. For the three geometrical configurations the peak of the electric field distribution is located outside the channel at $x \approx 5$ mm. The electric field goes to about zero at $x = 50$ mm, which is then the end of the acceleration region. Raitses *et al* obtained similar results with a 2 kW HT of which the channel width could be changed with ceramic spacers [16]. They examined two geometries: one with a h to d ratio close to the standard one and another one with a larger ratio. The plasma potential profile was measured inside and outside the channel by means of an emissive probe. The potential drop was weaker for the 'narrow' channel, however, the electric field was stronger. They also observed an outward shift of the electric field profile with the narrow channel, which is not noticed in this study.

A 4-grid repulsing potential analyser (RPA) was used to determine the ion energy distribution function (EDF) in the plume far-field of the PPI thruster [9]. The RPA probe acts as a high-pass filter: only ions with voltages, that is energy-to-charge ratios, greater than the repeller grid voltage can pass and reach the collection electrode. The potential of the ion retarding grid is then varied while monitoring the ion current incident on the collector; thus data are obtained as I versus V. The negative derivative of the $I(V)$ trace is proportional to the EDF [17]. Note that our RPA provides the ion energy with respect to ground.

The RPA device was placed 70 cm behind the PPI thruster exit plane along the thruster centreline. The voltage resolution was 1 V. The I–V trace was smoothed and interpolated with a cubic spline function before computing the derivative. The thruster was fired at 250 V. The graph in figure 9 shows the influence of the HT channel geometry on the most probable energy of the ion EDF. RPA measurement outcome is in agreement with LIF data: the ion kinetic energy increases significantly when h is doubled. For the S_0 to $2S_0$ transition, the gap is 26 V at 250 V applied voltage. One obtains 23 V with the LIF tool, see figure 8. RPA data also confirm the kinetic energy spread decreases when the channel cross-section area increases.

5. Plasma–wall interaction

After a critical examination of ionization and acceleration processes as a function of the thruster channel width, it is worth studying the influence of the geometry on plasma–surface interaction inside the channel. Two quantities are therefore of prime importance, namely the wall temperature and the energy flux to the walls.

5.1. Steady-state temperature

The equilibrium temperature of both the internal and external Al_2O_3 channel walls was determined by means of calibrated thermal imaging. The discharge voltage was set to 200 V and the xenon flow was adjusted around 1 mg s^{-1} to keep the discharge current constant at 1.1 A. Experiments were therefore performed at a fixed input power of 220 W.

Table 1. Equilibrium temperature of the Al_2O_3 channel walls for the three Hall thruster geometries (200 V, 220 W, ∼1 mg s^{-1}).

Geometry	Inner wall temperature (K)	Outer wall temperature (K)
S_0	860	722
$2S_0$	796	666
$3S_0$	770	605

Table 2. Energy flux to the walls q_p and power losses for the three Hall thruster geometries (200 V, 220 W, ∼1 mg s^{-1}).

Geometry	q_p (W cm^{-2}) Inner wall	q_p (W cm^{-2}) Outer wall	Power losses (W)
S_0	19.8	7.0	87
$2S_0$	18.0	6.0	72
$3S_0$	16.5	5.7	63

HT infrared image acquisition was accomplished with a calibrated infrared camera suited for the in the 8–9 μm domain [18]. The camera covers a temperature range from −20 to 1500 °C. Experiments were conducted in the NExET test bench with the infrared camera located in front of the PPI thruster at 1.5 m. Observation was carried out through a CaF_2 window. In order to enable absolute temperature determination for the thruster channel walls the normal spectral emissivity of the Al_2O_3 ceramic material was measured in air as a function of temperature. Within the 8–9 μm spectral band the emissivity does not change much with temperature. The mean emissivity is 1. The steady-state temperature of the inner and outer walls is given in table 1 for the three-channel configurations. The temperature of the internal wall $T_{\rm int}$ is always higher than the external wall $T_{\rm ext}$ because it is more difficult for the former to evacuate heat [18]. The temperature of the inner and outer channel walls decreases when the channel is widened. A low temperature means less thermal constraint on the thruster components. The drop in the wall temperature with the channel width is first a direct consequence of a geometrical effect. As confirmed by numerical simulations with a simplified thermal model of the thruster assembly, keeping the energy flux to the walls unchanged, the equilibrium temperature decreases when h increases due to a change in the geometrical view factors. The latter govern heat exchanges in a HT as only radiative transfers play a role. Simulations also confirm $T_{\rm ext} < T_{\rm int}$. Moreover, they indicate the temperature gap between S_0 and $2S_0$ is larger than the gap between $2S_0$ and $3S_0$. The remaining question at this stage concerns the possible link between the observed drop in wall temperature with the channel size and a decrease in the energy flux deposited by the plasma onto the walls.

5.2. *Wall losses*

The energy flux deposited by the plasma onto the channel wall can be assessed by combining temperature measurements with a thermal model [19, 20]. A time-dependent thermal model of a Hall effect thruster channel relies on the energy conservation equation and a set of simplifying assumptions [19]. Radiative transfers are treated following the approach of radiation exchange in a thermal enclosure. The latter is here composed of three surfaces that are individually isothermal: inner wall, outer wall and back wall. Radiative fluxes are then computed by means of grey body configuration factors. Heat conduction through channel walls is also taken into account. Boundary conditions correspond to the temperature of adjoining elements which is measured with thermocouples. To compute the temperature of a given channel section implies knowing at each time step the temperature of the two other parts as well as the distribution of the energy flux q_p. Here, numerical simulations use, as input data, temperature fields measured by thermal imaging. Advantages of this semi-empirical approach are twofold, namely it allows drastic reduction of the number of parameters and it brings the simulations closer to the real thermal behaviour of the thruster. The energy deposited by the plasma q_p is obtained by adjusting in an iterative manner the calculated time-dependent temperature profile to the one measured by means of calibrated infrared imaging [19, 20].

For a fixed input power, the energy flux deposited by the plasma onto channel walls q_p decreases with h for both the internal and the outer wall as can be seen in table 2. Results demonstrate the observed decrease in wall temperature is not only due to a geometrical effect (view factors) but also a change in energy flux. The amount of power lost to the walls can be computed: $P_{\rm wall} = q_{p,\rm ext} \times S_{\rm ext} + q_{p,\rm int} \times S_{\rm int}$. The surface onto which the power is deposited by charge particles is given by $S = \pi d L_{\rm loss}$, where $L_{\rm loss}$ is the length along which ion and electron bombardment is large. For a HT plasma–wall interaction is concentrated in the final section of the channel. For the PPI, one finds $L_{\rm loss} \approx 3$ mm. Results are shown in table 2. Power losses decrease when h increases. With the S_0 configuration, $P_{\rm wall}$ reaches 40% of the input power whereas $P_{\rm wall}$ represents 29% of the applied power for the $3S_0$.

6. Discussions

Two mechanisms can be put forward to explain the impact of the channel cross-section area on operating envelope and ionization and acceleration efficiency.

First, it is related to a purely geometrical effect. The surface-to-volume ratio, which is $2/h$, corresponds to a good approximation of the ratio of plasma losses to plasma production [5]. Indeed, for a low-pressure plasma, charged particles are produced in the bulk and lost onto surfaces. When increasing the channel width h ion production is therefore favoured. Wall-loss reduction also explains the fact that the discharge can be maintained at low power and the fact that the channel can endure high-power operation. Finally, a larger fraction of energy supplied to the device can be converted into axial ion motion when h is increased.

The second mechanism is linked to the magnetized area the plasma is exposed to. As exemplified in figure 2, stretching the channel in the radial direction makes the magnetic field intensity greater in the wall vicinity. The magnetic field gradient in the radial direction is stronger, which enhances the magnetic mirror effect [21]. The magnetic mirror ratio, i.e. the ratio of the magnetic field near the wall to the magnetic field in the centre of channel, increases with h. For the internal

wall at the channel exit plane it equals 1.2, 1.9 and 3.2 for the S_0, $2S_0$ and $3S_0$ geometry, respectively. Values are similar for the external wall. The magnetic confinement of charged particle inside the channel improves with h. Therefore, propellant utilization improves and plasma–wall interaction further reduces [22].

7. Conclusion and prospects

Enlarging the channel of a low-power HT enhances ionization and acceleration processes and broadens the operating envelope. Two mechanisms are proposed to explain experimental facts. First, the surface-to-volume ratio decreases with h, which reduces wall-losses. Second, the magnetic field strength near the walls increases with h, which leads to a better plasma confinement. We naturally expect an increase in the thrust level and a significant amelioration of the thrust efficiency when making larger the channel cross-section area. One of the next experiments will therefore consist in accurately measuring the thrust of the PPI Hall thruster for the three configurations. This work brings a means for improvement of the performance level of low-power HTs. It shows that the linear scaling of h with d should be modified for small thrusters. However, it does not warrant that the method can be successfully applied to large size devices. The surface-to-volume ratio is already great for high-power thrusters. Moreover, technological constraints could appear due to the use of coils along with an iron circuit to produce the magnetic field.

Acknowledgments

This study was performed within the framework of the CNRS/CNES/SNECMA/Universities joint-research program GDR 3161 entitled ‘Propulsion par plasma dans l’espace’. The skillful technical assistance of L Peilleron and E Labrude was greatly appreciated. The authors gratefully acknowledge stimulating discussion with Dr M Guyot from the GEMaC laboratory, who designed and built the PPI Hall thruster.

References

[1] Zhurin V V, Kaufmann H R and Robinson R S 1999 *Plasma Sources Sci. Technol.* **8** R1
[2] Goebel D M and Katz I 2008 *Fundamentals of Electric Propulsion* (Hoboken, NJ: Wiley)
[3] Wallace N C and Fehringer M 2009 *Proc. 31st Int. Electric Propulsion Conf. (Ann Arbor, MI)* IEPC paper 09-269
[4] Witzberger K E and Manzella D 2005 *Proc. 41st Joint Propulsion Conf. (Tucson, AZ)* AIAA paper 11-019
[5] Dannenmayer K and Mazouffre S 2011 *J. Propul. Power* **27** 236
[6] Raitses Y, Ashkenazy and Guelman M 1998 *J. Propul. Power* **14** 247
[7] Guyot M, Renaudin P and Boniface C 2007 *Patent FR* 07 05658
[8] Guyot M *et al* 2008 *Proc. 5th Int. Spacecraft Propulsion Conf. (Heraklion, Crete)*
[9] Lejeune A, Dannenmayer K, Bourgeois G, Mazouffre S, Guyot M and Denise S 2011 *Proc. 32nd Int. Electric Propulsion Conf. (Wiesbaden, Germany)* IEPC paper 11-019
[10] Gascon N, Dudeck M and Barral S 2003 *Phys. Plasmas* **10** 4123
[11] Dannenmayer K, Kudrna P, Tichý M and Mazouffre S 2012 *Plasma Sources Sci. Technol.* submitted
[12] Brown D L, Larson C W, Beal B E and Gallimore A 2009 *J. Propul. Power* **25** 1163
[13] Hofer R R, Jankovsky and Gallimore A D 2006 *J. Propul. Power* **22** 721
[14] Mazouffre S, Kulaev V and Pérez-Luna J 2009 *Plasma Sources Sci. Technol.* **18** 034022
[15] Gawron D, Mazouffre S, Sadeghi N and Héron A 2008 *Plasma Sources Sci. Technol.* **17** 025001
[16] Raitses Y, Staack D, Keidar M and Fisch N J 2005 *Phys. Plasmas* **12** 057104
[17] Böhm C and Perrin J 1993 *Rev. Sci. Instrum.* **64** 31
[18] Mazouffre S, Echegut P and Dudeck M 2007 *Plasma Sources Sci. Technol.* **16** 13
[19] Mazouffre S, Pérez Luna J and Dannenmayer K 2007 *J. Appl. Phys.* **102** 023304
[20] Mazouffre S, Dannenmayer K and Blank C 2011 *Phys. Plasmas* **18** 064501
[21] Keidar M and Boyd I D 2005 *Appl. Phys. Lett.* **87** 121501
[22] King L B 2005 *Proc. 29th Int. Electric Propulsion Conf. (Princeton, NJ)* IEPC paper 05-258